Journal of Sound and Vibration 326 (2009) 321–331

Contents lists available at ScienceDirect

Journal of Sound and Vibration

journal homepage: www.elsevier.com/locate/jsvi

Dynamic response of a shallow arch under end moments

Jen-San Chen *, Wei-Chia Ro

Department of Mechanical Engineering, National Taiwan University, Taipei 10617, Taiwan

ARTICLE INFO

Article history:
Received 2 November 2008
Received in revised form
26 April 2009
Accepted 2 May 2009
Handling Editor: L.G. Tham
Available online 2 June 2009

ABSTRACT

In this paper we study the dynamic response of a pinned shallow arch subjected to a pair of equal and opposite end moments suddenly. An experimental setup is designed to measure both the static deflection and dynamic response of the loaded arch. The dynamic buckling load as a function of the rise parameter is of particular interest. In order to theoretically identify the necessary and sufficient condition for dynamic snap-through, an accurate estimate of the system damping is required. This, however, proves to be a difficult task. A more practical approach is to adopt a sufficient condition which ensures that the arch will be safe from dynamic snapping. This condition leads to a lower bound of the dynamic critical load. As long as the end moments are smaller than this lower bound, it is guaranteed that the arch will not snap dynamically no matter what the system damping may be. For an arch with rise parameter greater than 6.55, it is shown that a closed-form expression of this lower bound of dynamic critical load can be derived. This simple formula should prove useful to design engineers.

1. Introduction

The prediction of snap-through buckling load of a shallow arch is a classic problem in applied mechanics. Previous research works available in the literature can be divided into three groups based on the type of external loads. In the first group the external loads are applied in the form of lateral forces on the arch. The lateral forces can be concentrated or distributed, space-fixed or moving, quasi-static or time-varying. For a complete review of the previous works of this group up to 1990, the readers are referred to the two books by Simitses [1,2]. Several more recent works can be found in [3]. In particular, Pi and Bradford [4] and Chen et al. [5] studied the dynamic snapping of a shallow arch under a suddenly applied concentrated force at the mid-point of the arch.

In the second group the external load is applied longitudinally at the ends. Although internal resonance is of primary interest, snap-through buckling is also possible by this type of loading. For the subject of internal resonance due to longitudinal force a fairly comprehensive reference list can be found in [6]. Snap-through buckling caused by harmonic longitudinal excitation was demonstrated by Chen and Chang [7].

In the third group, the shallow arch is loaded by a pair of equal and opposite moments at the two ends of the shallow arch. Plaut [8] appears to be the first author studying this problem, in which he derived the optimal design for stability for an arch under end moments. Recently, Chen and Lin [9] and Plaut [10] presented an exact static critical load for a pinned shallow arch under end moments. In practical applications it is more likely that the end moments, which are proportional to the actuating voltage in piezoelectric switching devices [11], are applied suddenly instead of quasi-statically. In such a case the shallow arch may snap dynamically and the associated buckling load is in general different from its quasi-static

* Corresponding author.
E-mail address: jschen@ntu.edu.tw (J.-S. Chen).

0022-460X/$ - see front matter © 2009 Elsevier Ltd. All rights reserved.
doi:10.1016/j.jsv.2009.05.002

counterpart. In this paper we extend our previous work on quasi-static loading [9] to the dynamic case when the shallow arch is loaded suddenly by a pair of equal and opposite end moments. Both theoretical and experimental methods are adopted and the results are compared.

2. Equations of motion

We consider a pinned shallow arch loaded suddenly by a pair of equal and opposite end moments, as shown in Fig. 1. The equation of motion of the loaded arch can be written as

$$\rho A y_{,tt} + EI(y - y_0)_{,xxxx} - p^* y_{,xx} + M^* H(t)[-\delta^{*'}(x) + \delta^{*'}(x - L)] = 0 \tag{1}$$

p^* is the axial force due to the stretching of the neutral axis,

$$p^* = \frac{AE}{2L}\int_0^L (y_{,x}^2 - y_{0,x}^2)\,\mathrm{d}x \tag{2}$$

ρ and E are mass density and Young's modulus. A and I are area and moment of inertia of the cross section. L is the distance between the two pinned-ends. x and t are the longitudinal position and time. $y_0(x)$ and $y(x,t)$ are the initial (unstrained) and the deformed shapes of the arch, both measured from the same base plane. M^* is the magnitude of the end moments. $\delta^{*'}$ is the derivative of the Dirac delta function with respect to x. $H(t)$ is the Heaviside step function.

Eqs. (1) and (2) can be non-dimensionalized to the forms

$$u_{,\tau\tau} + (u - u_0)_{,\xi\xi\xi\xi} - p u_{,\xi\xi} + \frac{\pi}{4} M H(\tau)[-\delta'(\xi) + \delta'(\xi - \pi)] = 0 \tag{3}$$

$$p = \frac{1}{2\pi}\int_0^\pi (u_{,\xi}^2 - u_{0,\xi}^2)\,\mathrm{d}\xi \tag{4}$$

The dimensionless parameters are related to their physical counterparts in the following forms:

$$(u, u_0) = \frac{1}{r}(y, y_0), \quad \xi = \frac{\pi x}{L}, \quad \tau = \frac{\pi^2 t}{L^2}\sqrt{\frac{EI}{A\rho}}, \quad p = \frac{p^* L^2}{\pi^2 EI}$$

$$M = \frac{4M^* L^2}{\pi^3 EIr}, \quad \delta' = \frac{L^2}{\pi^2}\delta^{*'}, \quad \omega = \frac{L^2}{\pi^2}\sqrt{\frac{A\rho}{EI}}\omega^*, \quad \mu = \frac{L^2\mu^*}{\pi^2\rho A r}\sqrt{\frac{\rho}{E}}$$

where $r = \sqrt{A/I}$ is the radius of gyration of the cross section. The parameters μ and ω are the damping and natural frequency of the arch, which will be discussed later. The boundary conditions for u at $\xi = 0$ and π are

$$u(0) - u_0(0) = u_{,\xi\xi}(0) - u_{0,\xi\xi}(0) = u(\pi) - u_0(\pi) = u_{,\xi\xi}(\pi) - u_{0,\xi\xi}(\pi) = 0 \tag{5}$$

The initial and deformed shapes of the arch are assumed to be in the forms

$$u_0(\xi) = h \sin \xi \tag{6}$$

$$u(\xi, \tau) = \lim_{N\to\infty}\sum_{n=1}^{N} \alpha_n(\tau)\sin n\xi \tag{7}$$

N is the number of modes used in the series (7). h is the arch height, sometimes called the rise parameter. After substituting Eqs. (6) and (7) into (3) and(4) we obtain the following equations for α_n:

$$\ddot{\alpha}_n = -n^4\alpha_n - n^2 p\alpha_n - q_n, \quad n = 1, 2, 3, \ldots \tag{8}$$

where

$$p = \frac{1}{4}\sum_{k=1}^{\infty} k^2\alpha_k^2 - \frac{h^2}{4} \tag{9}$$

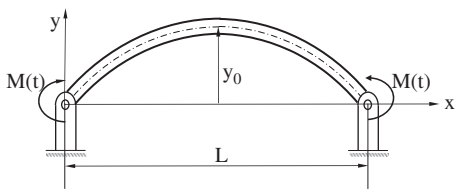

Fig. 1. A shallow arch loaded by a pair of equal and opposite end moments.

$$q_1 = M - h \tag{10}$$

$$q_n = 0, \quad n = 2,4,6,\ldots \tag{11}$$

$$q_n = nM, \quad n = 3,5,7,\ldots \tag{12}$$

The overhead dot in Eq. (8) represents differentiation with respect to τ. The arch is unstrained before time $\tau = 0$.

In the above formulation we include the moments in the equation of motion (3) instead of the boundary conditions. As a result the assumed functions in the infinite series (7) satisfy all the boundary conditions. A slightly different formulation is to include the moments in the boundary conditions and exclude them from the equation of motion. In this alternative approach the series (7) can still be used because the assumed functions satisfy the geometric boundary conditions, although not the natural boundary conditions involving the applied moments. After integrating by parts twice as in the usual Galerkin's procedure, the end moments will be incorporated into the discretized equations (8)–(12) automatically. These two approaches produce exactly the same result.

3. Equilibrium configurations

By neglecting the acceleration term in Eq. (8) we can solve for the equilibrium configurations. There are two types of solutions.

(1) *Symmetrical solution*: $\alpha_{2i} = 0$, where $i = 1,2,3,\ldots$. The remaining coordinates α_{2i+1} can be related to α_1 by eliminating p from the two equations in (8) for $n = 1$ and $2i+1$,

$$\alpha_{2i+1} = \frac{-\alpha_1 q_{2i+1}}{(2i+1)^2[4i(i+1)\alpha_1 - q_1]}, \quad i = 1,2,3,\ldots \tag{13}$$

α_1 can be solved by substituting Eq. (13) into Eq. (8) for $n = 1$, which becomes

$$\alpha_1 + \frac{\alpha_1}{4}(\alpha_1^2 - h^2) + q_1 + \sum_{i=1}^{\infty}\left\{\frac{q_{2i+1}^2 \alpha_1^3}{4(2i+1)^2[4i(i+1)\alpha_1 - q_1]^2}\right\} = 0 \tag{14}$$

(2) *Unsymmetrical solution*: $\alpha_{2j} \neq 0$ for some j, and all other $\alpha_{2i} = 0$, $i = 1,2,3,\ldots, i \neq j$. For this type of solution we can solve for α_1, α_3, α_5, etc., exactly as

$$\alpha_i = \frac{q_i}{i^2[4j^2 - i^2]}, \quad i = 1,3,5,\ldots \tag{15}$$

α_{2j} can be obtained from the following equation:

$$\alpha_{2j} = \pm\frac{1}{2j}\sqrt{h^2 - 16j^2 - \sum_{i=1,3,5,\ldots}^{\infty} \frac{q_i^2}{i^2[4j^2 - i^2]^2}}, \quad j = 1,2,3,\ldots \tag{16}$$

It is noted that the coordinates α_i of an unsymmetrical solution can be written in closed forms as in Eqs. (15) and (16), while α_i of a symmetrical solution can only be obtained numerically from Eq. (14).

In the case when $M = 0$, there are two types of symmetrical solutions, i.e., three one-mode solutions (P_0, P_1^+, and P_1^-) involving α_1 only, and pairs of two-mode solutions ($P_{1(2j+1)}^+$ and $P_{1(2j+1)}^-$, denoted collectively as $P_{1(2j+1)}^{\pm}$) involving two coordinates α_1 and α_{2j+1}. On the other hand, the unsymmetrical solutions always involve two coordinates α_1 and α_{2j}, denoted as $P_{1(2j)}^{\pm}$. P_0 represents the original shape. P_1^- is another stable configuration on the other side of the base plane. P_1^+ is an unstable position between P_0 and P_1^-. All two-mode solutions, symmetrical or unsymmetrical, are unstable.

As M increases from zero all symmetrical (unsymmetrical) solutions remain symmetrical (unsymmetrical), although all solutions involve infinite number of harmonic components. However, for simplicity we still use the notations P_0, P_1^+, P_1^-, and $P_{1j}^{\pm}$ for the case $M = 0$ to name the solutions for $M \neq 0$ even if they are no longer one- or two-mode solutions.

4. Natural frequencies

The natural frequencies ω_n of the two stable equilibrium positions P_0 and P_1^- when the arch is loaded by end moments can be calculated as follows. First of all we denote the coordinates of the stable position as α_n^s, which can be calculated from Eqs. (13) and (14). By superposing a small perturbations $\varphi_n(\tau)$ onto α_n^s, and substituting the perturbed coordinates $\alpha_n(\tau) = \alpha_n^s + \varphi_n(\tau)$ into Eq. (8), retaining only the linear terms, the linearized equations can be written as

$$\ddot{\varphi}_1 = -\varphi_1\left\{\frac{1}{4}\left[4 + 3(\alpha_1^s)^2 + \sum_{k=3,5,\ldots}^{\infty} k^2(\alpha_k^s)^2 - h^2\right]\right\} - \frac{\alpha_1^s}{2}\sum_{k=3,5,\ldots}^{\infty} k^2 \alpha_k^s \varphi_k \tag{17}$$

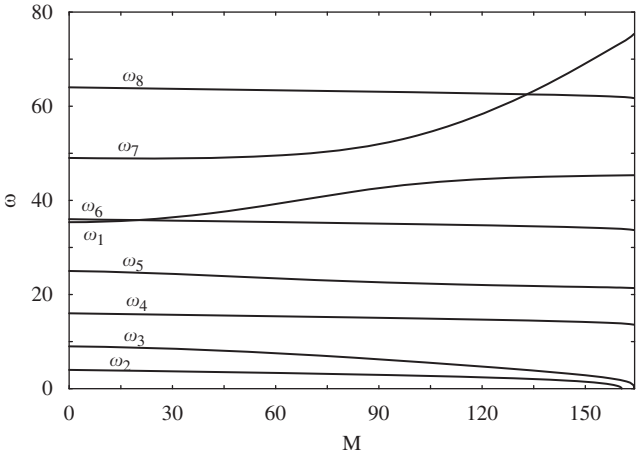

Fig. 2. Natural frequency loci as the end moment M increases.

$$\ddot{\varphi}_n = -\varphi_n\left\{n^4 + \frac{n^2}{4}\left[\sum_{k=1,3,\ldots}^{\infty} k^2(\alpha_k^s)^2 - h^2\right]\right\} - \frac{n^2\alpha_n^s}{2}\sum_{k=1,3,\ldots}^{\infty} k^2\alpha_k^s\varphi_k, \quad n = 3,5,\ldots \tag{18}$$

$$\ddot{\varphi}_n = -\varphi_n\left\{n^4 + \frac{n^2}{4}\left[\sum_{k=1,3,\ldots}^{\infty} k^2(\alpha_k^s)^2 - h^2\right]\right\}, \quad n = 2,4,\ldots \tag{19}$$

From Eqs. (17)–(19), one can calculate the natural frequencies of the arch near a stable equilibrium position.

It is noted that in the case when the arch is unloaded and unstrained, $\alpha_1^s = h$ and all other $\alpha_n^s = 0$ for $n \neq 1$. As a consequence the natural frequency ω_n corresponding to the mode shape $\sin n\xi$ (for $n \neq 1$) is n^2, which is independent of the arch height h. On the other hand, the natural frequency ω_1 corresponding to mode shape $\sin\xi$ is $\sqrt{1+(h^2/2)}$, which is normally not the fundamental frequency. For instance when $h = 50$, the fundamental frequency is $\omega_2 = 4$. $\omega_1 = 35.4$ is the fifth natural frequency.

In the case when $M \neq 0$, Eq. (19) indicates that the modes with even number of n are decoupled from others. As a result the eigenvector corresponding to ω_{2n} has only a non-zero component φ_{2n}, and the mode shape remains to be $\sin 2n\xi$ as M increases. On the other hand, Eqs. (17) and (18) indicate that the modes with odd number of n involve all odd number of components in the eigenvectors.

In Fig. 2 we show the variation of the natural frequencies near position P_0 when the load M increases from 0 to 170 for an arch with $h = 50$. It is observed that the frequency loci of the even number of modes, ω_2, ω_4, etc., decrease with M. In particular, the fundamental frequency ω_2 vanishes at $M = 161$, which is the static critical load. For M greater than 161, position P_0 becomes unstable and the calculated natural frequencies become meaningless. On the other hand, the frequency loci of the odd number of modes may decrease (ω_3 and ω_5) or increase (ω_1 and ω_7) with M. More calculations not shown here lead us to believe that for all the odd number of modes with frequencies higher than ω_1 when $M = 0$ the frequency loci will increase with M, and vice versa. Furthermore, Fig. 2 shows that the frequency loci ω_1 and ω_7 cross, instead of veering away from, the loci of ω_6 and ω_8 at $M = 19.7$ and 133, respectively.

5. Experimental verification

In order to examine the validity of the above formulation we design an experimental setup, as shown in Fig. 3, to measure the static and dynamic responses of an arch loaded by end moments. The measurement will be compared with numerical simulation based on Eqs. (8)–(12). The arch is made of brass strip with Young's modulus 101 GPa and mass density 8840 kg/m^3. The span length L of the arch is 44 cm and the cross section is 20 mm × 1.0 mm. Both ends of the curved beam are attached to roller bearings to simulate pinned condition. Attached to the outer race of the roller bearings are pulleys with radius of 2.05 cm. Cotton strings are fastened to and rounded around the pulleys on the arch ends and guided by another set of pulleys on the table as shown. At the end of the two strings is attached a hanging bucket. In the bucket we put in small steel screws as dead load. Each screw weighs 53 g and contributes 0.54 N cm of moment on each end. The empty bucket weighs 100 g.

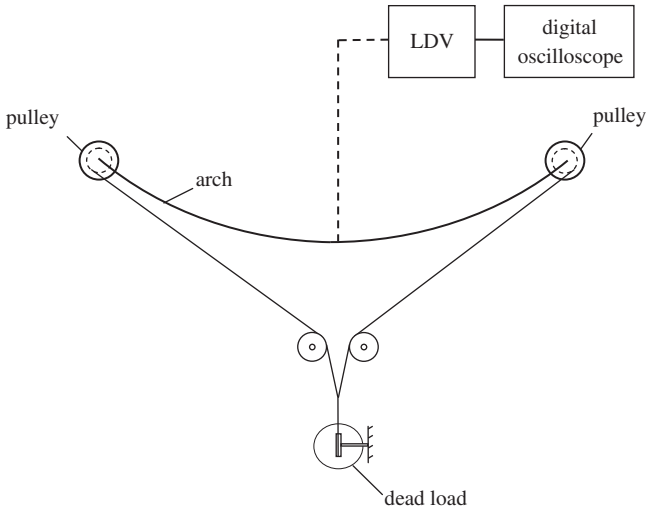

Fig. 3. Schematic diagram of the experimental setup.

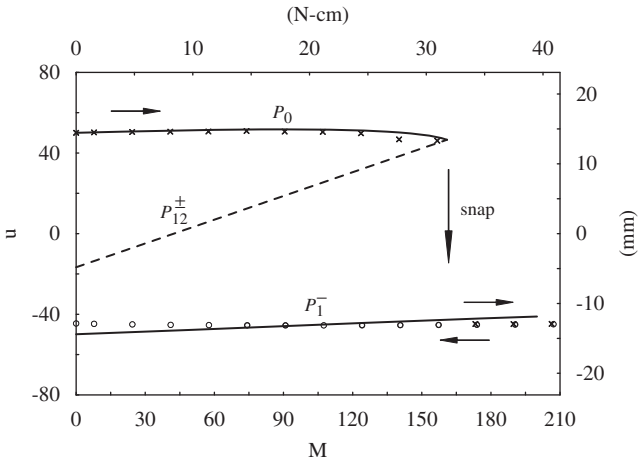

Fig. 4. Static deflection u at the midpoint of an arch with height $h = 50$ (14.4 mm) as a function of the end moment M. The symbols (×) and (○) record the deflections during loading and unloading processes, respectively.

5.1. Static deformation

We first measure the midpoint deflection of an arch with height $h = 50$ (14.4 mm) when the end moments are applied quasi-statically. We use a micro-stage on a vertical post to measure the displacement of the arch midpoint. Four screws are added to the bucket each time. As a consequence, the moment increment in the test is $\Delta M = 11$ (2.2 N cm). On the micro-stage we attach a metallic probe connected to a multimeter. An alarm will sound off when the probe touches the brass strip. The arrows in the figure indicate the direction of the applied load variation. For convenient reference, we present the measured results with both dimensionless parameters (left and bottom sides) and the physical ones (right and top sides). The same labeling style is adopted in all the figures involving experimental measurements.

In the first run of the test, the end moments are increased from zero until the arch snaps when $M = 175$ (35 N cm). The positions u of the midpoint are recorded in Fig. 4 as cross marks (×). After snapping, we continue to increase the end moments until $M = 205$ (41 N cm). In the second run of the test we reverse the loading direction by removing the screws from the bucket one by one until the bucket is empty. The displacement measurements in this unloading process are recorded by open circles (○).

Numerical predictions of the midpoint position based on the theory in Section 3 are plotted in Fig. 4 for comparison. Four modes ($N = 4$) are found to be enough to ensure convergence in static loading. The solid lines in the upper and lower branches represent the stable P_0 and P_1^- configurations. The dashed straight line represents the unstable $P_{12}^{\pm}$ configuration as defined in Section 3. Theoretical quasi-static snapping occurs when the deflection curve of $P_{12}^{\pm}$ intersects those of P_0 and

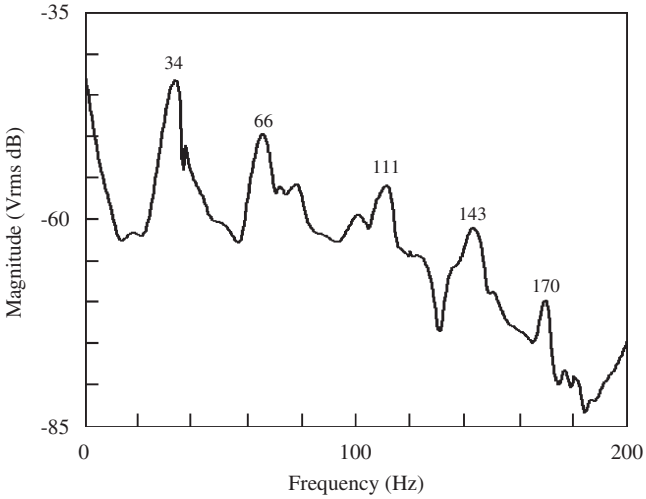

Fig. 5. Power spectrum of the free arch.

P_1^-. The static critical end moment (as $N\to\infty$) is predicted in [9] as

$$M_{cr}^{S\pm}=\frac{16}{9\pi^2}\left[4h\pm\sqrt{(16+18\pi^2)h^2-324\pi^2}\right] \tag{20}$$

For the specimen in the test, the theoretical critical moment is $M_{cr}^{S+}=161$ (32 N cm). The "+" sign in M_{cr}^{S+} indicates that the critical load snaps the arch from P_0 to P_1^-.

From Fig. 4 we observe that the displacement measurements follow the theoretical load–deflection curve closely in both branches, and snapping occurs at the predicted critical load within the accuracy limit of our test ($\Delta M=11$). This satisfactory agreement between experiment and theory enhance our confidence in the mathematical formulation and the material constants we adopt from engineering handbooks.

5.2. Measurement of natural frequencies

We use an LDV system (Polytec OFV508/2802) to measure the natural frequencies of the shallow arch. The laser beam is shone on a point of the arch, as shown in Fig. 2. In the experiment the target point is not necessarily the midpoint. After hitting the arch with a small rod, the response signal is fed into a spectrum analyzer (HP35665A) to calculate its power spectrum. Fig. 5 is an example power spectrum when the arch is unloaded. The first five natural frequencies are detected at 34, 66, 111, 143, and 170 Hz. The theoretical model predicts 32, 72, 129, 201, and 284 Hz. The discrepancy between experiment and theory are 4.4, 8.7, 13.6, 28.8, and 40.3 percent, respectively. Although the accuracy of the theoretical prediction deteriorates in the higher modes, the agreement is not so bad in the first three modes.

Our experience indicates that the rotary inertia of the end pulleys, which is ignored in the theoretical model, has a non-ignorable effect on the natural frequencies. The agreement between experiment and theory was terrible in our first design in which each end pulley weighs almost 0.7 kg. The discrepancy in the fundamental frequency ran as high as 48 percent with this design. After reducing the size of the pulley dramatically to 0.06 kg each through a finite element analysis, we see noticeable improvement in the agreement between experiment and theory.

5.3. Estimate of damping

To simulate the dynamic response of the arch under step end moments numerically, we have to estimate the damping of the arch assembly first. The dissipating mechanism of the system comes from the friction in the moving parts and the material damping in the arch. We assume that the damping mechanism is of the viscous type and modify Eq. (8) by adding damping parameters μ_n,

$$\ddot{\alpha}_n=-\mu_n\dot{\alpha}_n-n^4\alpha_n-n^2p\alpha_n-q_n,\quad n=1,2,3,\ldots \tag{21}$$

It is noted that Eq. (21) allows the damping parameters to be different for each mode.

We first pull the string attached to the hanging bucket a small distance and release. This action is equivalent to imposing a small rotation on both ends. We measure the transient response at the midpoint. The speed signal from the LDV system can be integrated to obtain the displacement history $u-u_0$ as shown by the solid line in Fig. 6. This transient response is

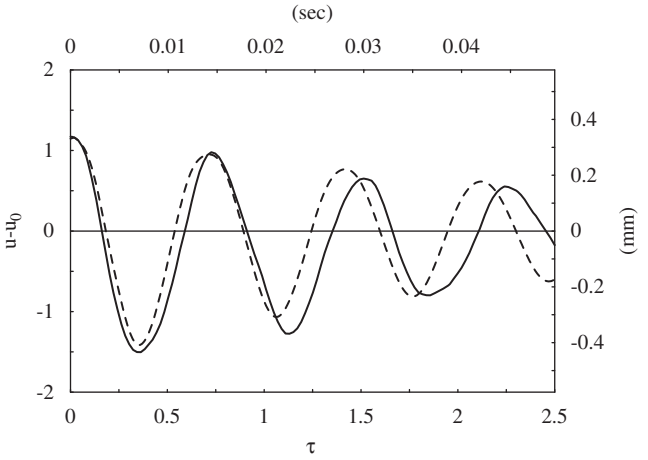

Fig. 6. Solid line is the measured lateral displacement history at the midpoint by imposing small rotations at both ends and release. Dashed line is the calculated response based on the estimated damping.

dominated by the mode $\sin 3\xi$ with frequency 66 Hz. We assume that this damped response can be simulated by retaining only μ_3 in Eq. (21). From the decaying rate between two consecutive peaks we can estimate the damping ratio of this mode, which is the ratio between μ_3 and a critical damping μ_{3c}, as 4 percent. This suggests that the arch system in our experiment can be considered as lightly damped. The critical damping μ_{3c} is obtained numerically by increasing μ_3 from zero gradually until the response ceases to oscillate. By this manner μ_{3c} and μ_3 are found to be 17.2 and 0.66, respectively. The numerical result obtained by integrating Eq. (21) based on this estimated damping ($\mu_3 = 0.66$) is plotted in Fig. 6 as dashed line to check the accuracy of this estimate. This logarithmic decrement method can be found in [12].

We assume that the damping ratios of all other modes are in the similar order of magnitude, i.e., 4 percent. By this bold assumption we can calculate μ_{nc} and μ_n accordingly. Whether they are good estimates can be judged in the following experiments.

5.4. Dynamic response under step end moments

In the first experiment on the dynamic response, we apply a smaller end moment $M = 37$ (7.4 N cm). The loaded bucket is released by hand suddenly to simulate a step load. The solid line in Fig. 7(a) represents the measured lateral position history u at the midpoint while the dashed line represents the numerical simulation based on Eq. (21). The response appears to be dominated by α_3. No dynamic snap-through occurs in this test. For the range of time in Fig. 7, it is found that 8 modes are sufficient in ensuring convergence. This means that the result from a 16-mode approximation is indistinguishable from the one from an 8-mode approximation. It is observed that the agreement between experiment and theory is quite good in the first five oscillations. After 0.1 s, however, the measured displacement appears to be stuck and ceases to oscillate. This suggests that the viscous damping model is inadequate in modeling the dynamic response when the vibration amplitude is too small. Instead, this sticky motion may be simulated better with a friction damping model, which will not be discussed in his paper.

In the second experiment we increase the end moment to 161 (32 N cm). In this test the arch is observed to snap to the other side directly, as shown by the solid line in Fig. 7(b). By comparing to the numerical simulation (dashed line) we observe that the theoretical model seems to be able to capture the essential feature of the response. In particular, the first reverse peak at $\tau = 4.5$ agrees with the experiment quite well. However, the height of the next peak is not as large as the measured one. This suggests that the system damping, which is estimated near the position P_0, is a little too large in predicting the response when the arch vibrates near another position P_1^-.

5.5. Measurement of dynamic snapping load

Following the above dynamic experiments, a question arises naturally regarding at exactly what end moment dynamic snap-through will start to occur. In order to answer this question, we prepare six specimens with arch heights $h = 20$, 30, 40, 50, 60, and 70. For each specimen we repeat the dynamic experiment by increasing the magnitude of the end moments incrementally by $\Delta M = 2.75$ until the arch snaps dynamically. The symbol " $\times$ " in Fig. 8 marks the smallest moment needed to snap the arch dynamically from position P_0 to P_1^- for each respective arch height.

The measured critical load can be compared with the numerical simulation based on Eq. (21). For each of these arch heights at hand, we increase the end moment incrementally by $\Delta M = 1$ and examine the history of coordinate α_1 up to $\tau = 100$. If at any time before $\tau = 100$ α_1 becomes negative, we say that the arch snaps dynamically. In reality, it is observed

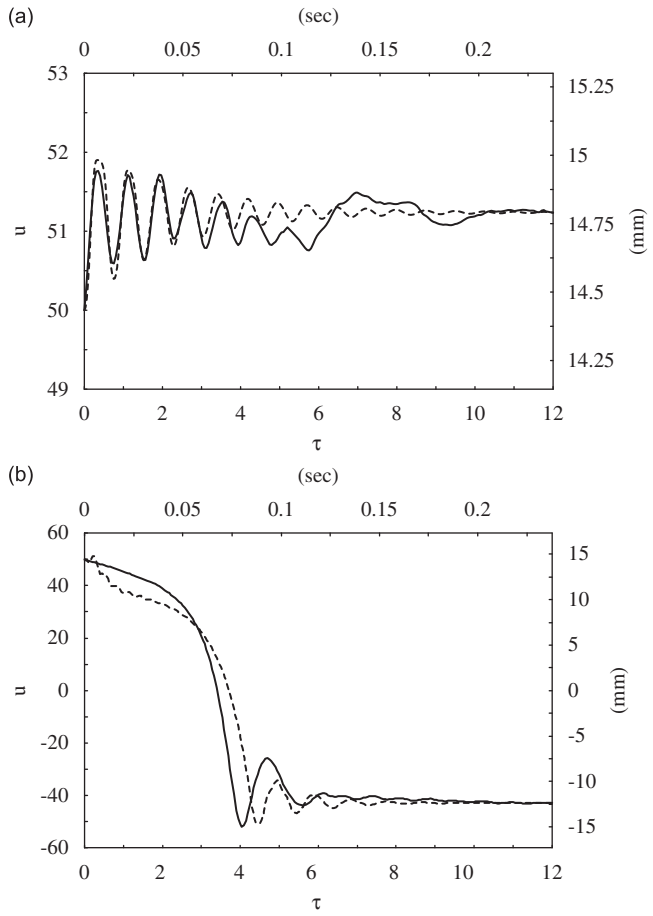

Fig. 7. Midpoint position history of the arch ($h = 50$) after the end moments are applied suddenly. The solid and dashed lines are the experimental and theoretical results, respectively: (a) $M = 37$ (7.4 N cm) and (b) $M = 161$ (32 N cm).

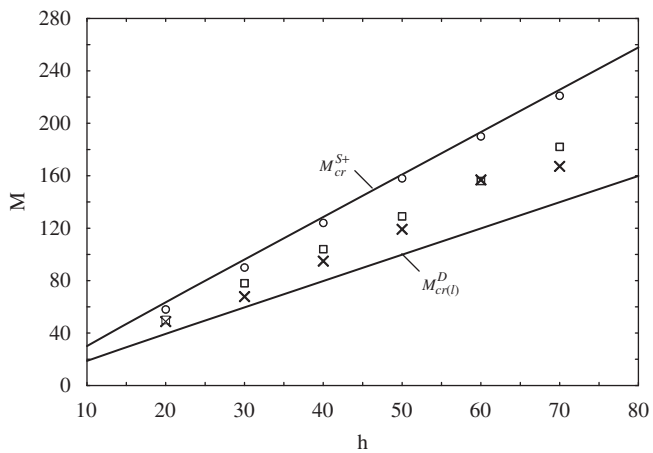

Fig. 8. Symbol × represents the experimentally determined dynamic critical load. Symbols ○ and □ represent the theoretical predictions based on 4 percent and 0 percent of system damping, respectively. The two critical conditions $M_{\mathrm{cr}(l)}^{D}$ and M_{cr}^{S+} are plotted for comparison.

that the arch reaches equilibrium state well before $\tau = 20$ in most of the cases. The smallest moment is then marked with open circle "○" in Fig. 8. It is observed that the numerical simulation overestimates the dynamic critical load by about 28 percent in each of the arch under test. This overestimation suggests that the system damping adopted in the calculation may be too large in predicting the dynamic critical load.

6. Total potentials

The calculation of the dynamic critical load as described in Fig. 8 is time-consuming. Besides, the numerical result is strongly dependent upon damping, which is in general difficult to estimate satisfactorily. In the following sections we endeavor to find a lower bound of the dynamic buckling load based on the total potential of the loaded arch. This lower bound offers us a more conservative estimate of the dynamic critical load and is immune from the inaccuracy of the estimated damping. This approach is considered to be more practical in engineering applications than the direct integration method. It will be shown that under certain condition the closed-form expression of this lower bound can even be obtained.

For dynamic snap-through to occur there must exist two stable equilibrium configurations after the step end moments are applied. While it is in general difficult to determine the necessary and sufficient condition for dynamic snap-through to occur, as explained in Section 5.5, it is possible to establish a sufficient condition against dynamic snap-through in terms of the total potential U of the loaded arch. The magnitude of the end moments which meets this sufficient condition is called the lower bound of the dynamic critical load in this paper. If the magnitude of the end moment is smaller than this lower bound, it is guaranteed that the arch will return to P_0 position after the transient vibration is settled by damping. On the other hand, there is no guarantee whether the arch will snap or not when the magnitude of the end moment is greater than this lower bound. This conservative lower bound can be determined from the condition that the energy barrier between the two stable positions becomes zero [2].

The dimensionless total potential U of an equilibrium configuration is defined as

$$U = U_s + U_m \tag{22}$$

where U_s is the strain energy of the deformed arch and U_m the potential corresponding to the end moments,

$$U_s = 2p^2 + \frac{2}{\pi}\int_0^{\pi}(u_{,\xi\xi} - u_{0,\xi\xi})^2\,\mathrm{d}\xi = 2p^2 + h^2 - 2h\alpha_1 + \sum_{n=1}^{\infty}[n^4\alpha_n^2] \tag{23}$$

$$U_m = 2M[u_{,\xi}(0) - u_{0,\xi}(0)] = 2M\left[\sum_{n=1,3,5,\ldots}^{\infty} n\alpha_n - h\right] \tag{24}$$

The relation between U and its physical counterpart U^* is

$$U^* = \frac{4AL^3U}{\pi^4EI^2}$$

The total potentials of the equilibrium configurations P_{1j}^+ and P_{1j}^- are equal, denoted as $U(P_{1j}^{\pm})$. In the case when the loaded arch possesses two-mode solutions, the energy barrier between the two stable configurations P_0 and P_1^- can be proved to be the total potential of $P_{12}^{\pm}$. In general this occurs when the arch height h is greater than 6.55 [9]. On the other hand for $h<6.55$ the energy barrier is the total potential of P_1^+. Since the heights of all the specimens tested in this paper are greater than 6.55, we focus our attention on this case.

Fig. 9 shows the total potentials $U(P_0)$, $U(P_1^+)$, and $U(P_{12}^{\pm})$, as calculated from Eqs. (22)–(24), as functions of M for an arch with $h = 50$. The total potentials of other unstable configurations, such as, $P_{13}^{\pm}$, $P_{14}^{\pm}$, etc., are beyond the range of the plot. The total potential $U(P_{12}^{\pm})$ meets line $U = 0$ when $M = 100$, which is the lower bound of the dynamic critical load $M_{\mathrm{cr}(l)}^D$. It is

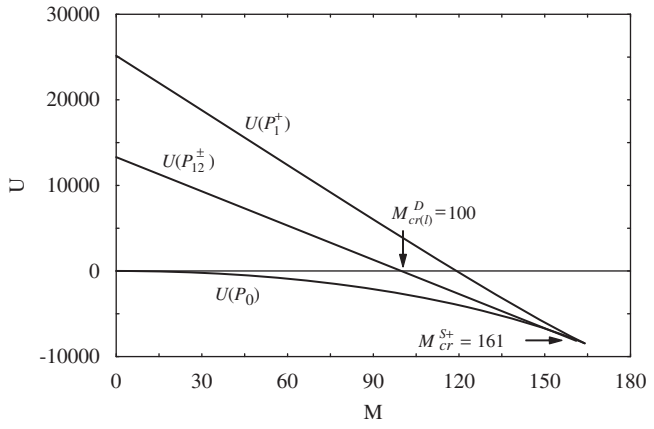

Fig. 9. Total potentials $U(P_0)$, $U(P_1^+)$, and $U(P_{12}^{\pm})$ as functions of M for a shallow arch with $h = 50$. The lower bound of the dynamic critical load $M_{\mathrm{cr}(l)}^D = 100$ corresponds to the situation when $U(P_{12}^{\pm})$ becomes zero.

noted that $U(P_{12}^{\pm})$ meets $U(P_0)$ when $M=161$, which is the static critical load M_{cr}^{S+}. For this arch with $h=50$ the lower bound of the dynamic critical load is 38 percent of M_{cr}^{S+}.

7. Exact lower bound of dynamic snapping load

It is noted that the curve $U(P_{12}^{\pm})$ in Fig. 9 appears to be a straight line. In this section we verify this observation analytically and derive the exact expression of the lower bound of the dynamic critical load. This is possible because the coordinates α_2 and α_{2i+1} of $P_{12}^{\pm}$ can be written in closed forms. From Eqs. (22)–(24) $U(P_{12}^{\pm})$ can be written as

$$U(P_{12}^{\pm}) = 32 + h^2 - 2h\alpha_1 - 2hM + 16\alpha_2^2 + \sum_{n=1,3,5,\ldots}^{\infty} [n^4\alpha_n^2 + 2nM\alpha_n] \tag{25}$$

It is noted that the α_i's in Eq. (25) are functions of M. After substituting α_2 from Eq. (16) and α_{2i+1} from Eq. (15) into Eq. (25), the total potential $U(P_{12}^{\pm})$ can be simplified to the following form:

$$U(P_{12}^{\pm}) = -\frac{8}{3}hM + \left(\frac{16}{3}h^2 - 32\right) \tag{26}$$

This confirms the observation in Fig. 9 that $U(P_{12}^{\pm})$ is a straight line. From the condition $U(P_{12}^{\pm})=0$ for the lower bound of the dynamic critical load, we can derive the exact expression of $M_{cr(l)}^{D}$ as

$$M_{cr(l)}^{D} = 2h - \frac{12}{h} \tag{27}$$

Both critical conditions for static (Eq. (20)) and dynamic (Eq. (27)) buckling are plotted in Fig. 8 to compare with the experimental and direct integration results. First of all, M_{cr}^{S+} can be considered as the upper bound of the dynamic critical load, i.e., the arch will definitely snap as long as the end moment is greater than M_{cr}^{S+}. This is only natural because the arch will settle to equilibrium state sooner or later. Secondly, $M_{cr(l)}^{D}$ indeed establishes a conservative lower bound of the dynamic critical load. In other words, for end moments smaller than $M_{cr(l)}^{D}$, it is guaranteed that the arch is safe from dynamic snapping. For end moments between $M_{cr(l)}^{D}$ and M_{cr}^{S+} the arch may or may not snap dynamically, depending upon the system damping. Thirdly, and somewhat surprisingly, for an arch with 4 percent of damping ratio the numerical prediction of dynamic critical moment is actually very close to the static critical load M_{cr}^{S+}. For instance, for the arch with $h=50$, direct integration predicts dynamic critical load at 159. This is only slightly smaller than the static critical load $M_{cr}^{S+}=161$. For an arch with smaller damping, it is expected that the dynamic critical load predicted via direct integration should be noticeably smaller than M_{cr}^{S+}. In a numerical experiment, we repeat the direct integration by removing the system damping altogether. The calculated dynamic critical loads are then marked with symbol "□". These undamped dynamic critical loads lie midway between $M_{cr(l)}^{D}$ and M_{cr}^{S+}. Moreover, they predict the real dynamic critical load even better than the ones taking into account the system damping estimated from experiment. This discouraging result stresses one more time the difficulty in estimating the damping of the system reasonably.

8. Conclusions

In this paper we study the dynamic in-plane snap-through of a shallow arch subjected to a pair of equal and opposite end moments suddenly. An experimental setup is designed to measure both the static deflection and dynamic response of the loaded arch. The dynamic critical load as a function of the arch height is of particular interest. Several conclusions can be summarized as follows:

(1) The static deflection measurements agree with the theoretical load–deflection relation and the static critical load quite well. This confirms that the mathematical formulation and the material constants adopted in the calculations are acceptable.
(2) An accurate estimate of the system damping is critical in predicting the dynamic response of the loaded arch. This, however, proves to be a difficult task. Our experimental results suggest that the viscous model of damping may be inadequate when the vibration amplitude becomes small. Furthermore, the damping parameters estimated near an equilibrium position may not be usable when the arch vibrates near another position. These difficulties render the numerical prediction of the necessary and sufficient condition for dynamic snap-through impractical.
(3) A more practical approach is to adopt a sufficient condition which ensures that the arch will be safe from dynamic snapping. This condition leads to a lower bound of the dynamic critical load. As long as the end moments are smaller than this lower bound, it is guaranteed that the arch will not snap dynamically no matter what the system damping may be.
(4) For an arch with height greater than 6.55, it is shown that closed-form expression of this lower bound of dynamic critical load can be found as in Eq. (27). This simple formula should prove useful to design engineers.

References

[1] G.J. Simitses, *Elastic Stability of Structures*, R.E. Krieger Publishing Co., Malabar, FL, 1986.
[2] G.J. Simitses, *Dynamic Stability of Suddenly Loaded Structures*, Springer, New York, 1990.
[3] N.J. Mallon, R.H.B. Fey, H. Nijmeijer, G.Q. Zhang, Dynamic buckling of a shallow arch under shock loading considering the effects of the arch shape, *International Journal of Non-Linear Mechanics* 41 (2006) 1057–1067.
[4] Y.-L. Pi, M.A. Bradford, Dynamic buckling of shallow pin-ended arches under a sudden central concentrated load, *Journal of Sound and Vibration* 317 (2008) 898–917.
[5] J.-S. Chen, W.-C. Ro, J.-S. Lin, Exact static and dynamic critical loads of a shallow arch under a point force at the midpoint, *International Journal of Non-Linear Mechanics* 44 (2009) 66–70.
[6] J.-S. Chen, C.-H. Yang, Experiment and theory on the nonlinear vibration of a shallow arch under harmonic excitation at the end, *ASME Journal of Applied Mechanics* 74 (2007) 1061–1070.
[7] J.-S. Chen, D.-W. Chang, Snapping of a shallow arch with harmonic excitation at one end, *ASME Journal of Vibration and Acoustics* 129 (2007) 514–519.
[8] R.H. Plaut, Optimal arch form for stability under end moments, *Proceedings of the 18th Midwestern Mechanics Conference*, Iowa City, IA, 1983, pp. 87–89.
[9] J.-S. Chen, J.-S. Lin, Exact critical loads for a pinned half-sine arch under end couples, *ASME Journal of Applied Mechanics* 72 (2005) 147–148.
[10] R.H. Plaut, Snap-through of shallow elastic arches under end moments, *ASME Journal of Applied Mechanics* 76 (2009) 014504.
[11] C. Maurini, J. Pouget, S. Vidoli, Distributed piezoelectric actuation of a bistable buckled beam, *European Journal of Mechanics A* 26 (2007) 837–853.
[12] S.S. Rao, *Mechanical Vibrations*, third ed., Addison-Wesley, Reading, MA, 1995.